

Flow-Based Characterization of Digital Rock Images Using Deep Learning

Naif J. Alqahtani, Traiwit Chung, Ying Da Wang, Ryan T. Armstrong, Pawel Swietojanski, and Peyman Mostaghimi, The University of New South Wales, Sydney, Australia

Summary

X-ray imaging of porous media has revolutionized the interpretation of various microscale phenomena in subsurface systems. The volumetric images acquired from this technology, known as digital rocks (DR), make it a suitable candidate for machine learning and computer-vision applications. The current routine DR frameworks involving image processing and modeling are susceptible to user bias and expensive computation requirements, especially for large domains. In comparison, the inference with trained machine-learning models can be significantly cheaper and computationally faster. Here we apply two popular convolutional neural network (ConvNet) architectures [residual network (ResNet) and ResNext] to learn the geometry of the pore space in 3D porous media images in a supervised learning scheme for flow-based characterization. The virtual permeability of the images to train the models is computed through a numerical simulation solver. Multiple ResNet variants are then trained to predict the continuous permeability value (regression). Our findings demonstrate the suitability of such networks to characterize volume images without having to resort to further ad-hoc and complex model adjustments. We show that training with richer representation of pore space improves the overall performance. We also compare the performance of the models statistically based on multiple metrics to assess the accuracy of the regression. The model inference of permeability from an unseen sandstone sample is executed on a standard workstation in less than 120 ms/sample and shows a score of 0.87 using explained variance score (EVS) metric, a mean absolute error (MAE) of 0.040 darcies, and 18.9% relative error in predicting the value of permeability compared to values acquired through simulation. Similar metrics are obtained when training with carbonate rock images. The training wall time and hyperparameters setting of the model are discussed. The findings of this study demonstrate the significant potential of machine learning for accurate DR analysis and rock typing while leveraging automation and scalability.

Introduction

Determination of permeability of porous media is one of the key practical interests in assessing subsurface reservoirs. The quantification of geomaterials permeability mathematically is not straightforward because permeability depends on the heterogeneity and complexity of such material's microstructure (Bear 1972). Many studies showed that absolute permeability is related to other petrophysical properties, such as porosity, pore geometry, connectivity, and tortuosity (Carman 1956; Bear 1972; Katz and Thompson 1986; Sahimi 2011). However, there is no direct correlation for estimating the permeability of porous media accurately without solving for flow at the microscale (Pan et al. 2001; Arns et al. 2004; Mostaghimi et al. 2013). With the emergence of high-resolution 3D imaging, an accurate geometry of microscale pores in earth materials, also known as DR, can be reliably obtained at a few micrometers or even submicrometer resolution (Coenen et al. 2004; Blunt et al. 2013). Such detailed data gives unparalleled knowledge for predicting macroscopic physical properties from the microstructural morphology of the rock using numerical simulations (Fredrich et al. 2006).

Modeling flow and transport at the pore scale involve solving governing fluid flow equations such as conservation of mass and momentum (Mostaghimi et al. 2017). The past two decades showed extraordinary advancement in numerical modeling methods of fluid flow in porous media. These methods can be classified into direct modeling methods and pore network modeling methods. Lattice-Boltzmann methods are well-known as one of the widely used methods for computing flow directly on reconstructed pore-scale images (Bhatnagar et al. 1954; Ferréol and Rothman 1995; Arns et al. 2004; Jin et al. 2004; Wang et al. 2019b). Other direct modeling methods involve medium discretization to solve the Navier-Stokes equation or Stokes equation for creeping flow (Mostaghimi et al. 2012, 2013) or to solve elliptic flow equations (Chung et al. 2019). Still, there are several potential drawbacks to direct modeling methods. Solving numerical simulation directly is often time-consuming and requires high computational capacity and an extensive memory allocation (White et al. 2006). Pore network modeling has been considered as an appealing alternative for direct numerical simulation (Silin and Patzek 2006; Al-Kharusi and Blunt 2007). The reason is because pore network modeling requires less computing capacity due to the simplified pore-space representation during reconstruction. An accurate simulation of fluid flow using pore network models requires a suitable representation that captures the essential morphological details of the pore space. However, most of the current models rely on assumptions that simplify the geometry of the rock and might be vague when defining what is considered pores or pore throat.

Following many breakthroughs in a variety of computer vision tasks in recent years, deep learning (DL) has become a popular research area. DL architectures have overwhelmingly surpassed the performance of the classic state-of-the-art models in computer vision including, but not limited to, image classification (Krizhevsky et al. 2012; Szegedy et al. 2015), object detection (Sermanet et al. 2013; Girshick et al. 2014), and semantic segmentation (Long et al. 2015; Lin et al. 2016). Subsequently, there has been a general interest in deploying DL on various digital inputs representing porous media. In particular, deep neural network architectures have been applied for DR image preprocessing and modeling; such applications include image resolution enhancement (Super Resolution; Kamrava et al. 2019a; Wang et al. 2019a; Niu et al. 2020b), image segmentation (Karimpouli and Tahmasebi 2019; Varfolomeev et al. 2019; Ar Rushood et al. 2020; Niu et al. 2020a), generating porous media (Mosser et al. 2017), and predictive modeling of physical properties (Alqahtani et al. 2018, 2020; Sudakov et al. 2019; Kamrava et al. 2019b).

ConvNets (Lecun et al. 1998) make the backbone of typical DL models. Such a model consists of a sequence of nonlinear transformations implemented as convolutional layers (i.e., layers with efficient weight sharing mechanism that allows reusing the same features across various spatial locations in an image). Depending on the task, the output of a ConvNet can model a categorical distribution over a set of mutually exclusive classes (classification) or estimate some continuous values (regression) (Belagiannis et al. 2015; Lathuilière et al. 2019). The model parameters are optimized such that they minimize some loss functions, which for regression problems is often

defined as least square error; that is, the measure of the difference between current model predictions and desired ground truth target predictions. A brief introduction for predicting several porous media properties using ConvNets is given in Alqahtani et al. (2020). We refer readers to Goodfellow et al. (2016) for further details about DL in general, and to Tahmasebi et al. (2020) and Wang et al. (2021) for DL in geoscience. With the advancement in computational capabilities and a better understanding of learning dynamics behind DL models, the architecture of ConvNets became deeper, allowing the discover of more abstract features. Many architecture adjustments for boosting the performance of DL models made significant improvements to ordinary/shallow ConvNets performance, including Inception by Simonyan and Zisserman (2014), VGG-16 by Szegedy et al. (2015), and ResNets by He et al. (2016). ConvNets can work with arbitrary spatial dimensions, including volumetric 3D images by using 3D kernels on 3D images (Maturana and Scherer 2015).

During the last few years, there have been efforts directed toward deploying machine learning as regression models for predicting porous media physical properties. Many of these efforts showed ConvNets among the best performing models. Some of the previous efforts are listed in **Table 1**. While many of these studies introduced new ideas, frameworks, and important findings, there is still a general lack of understanding of how accurate and reliable the predictions can become. The performance of DL models is mainly subjective to the complexity of data (morphology, heterogeneity, etc.), the size of data set available for training, and the architecture. We find that the majority of studies in Table 1 have been trained or tested on one or two samples; if not, synthetically generated images are used. This may not reflect performance on more heterogenous rocks. Also, the architecture of all models in Table 1 are relatively shallow (typically one to eight convolutional layers), which might not unlock the full potential of DL models if recent advancements of deeper state-of-the-art architecture are considered.

Research Paper	Type of Data	Training Image Size\Size of Data Set	Training and Testing Split	ConvNet Architecture	Accuracy Metrics	Summary of Reported Accuracy Metrics on the Testing Data Set	Main Findings\Remarks
Hong and Liu (2020)	Training: Coconino sandstone Testing: Bentheim sandstone	100 ³ 3,215 samples	98 to 2%	3D ConvNet three convolutional layers	R^2 —coefficient of determination root mean squared error (RMSE)—standard deviation	Testing: mean R^2 : 0.866; mean RMSE: 832 md; external sample Bentheim sandstone: mean R^2 : 0.694; mean RMSE: 2673 md	3D ConvNets show a relatively good fit for subvolumes obtained from same rock. Accuracy on external samples is not optimal.
Kamrava et al. (2019b)	Training: Berea sandstone Testing: Fontainebleau sandstone	200 ³ 510 sandstone samples + 400 synthetically generated samples	Not mentioned	3D ConvNet number of layers is not mentioned	R^2 —coefficient of determination	Berea: R^2 : 0.91 Fontainebleau: R^2 : 0.90	3D ConvNets can learn morphology and link it to permeability.
Sudakov et al. (2019)	One Berea sandstone sample	100 ³ 9,261 samples	90 to 10%	Different ML methods 2D ConvNet-10 convolutional layers 3D ConvNet-four convolutional layers	Average absolute error normalized by the spread of 1st and 99th percentile of permeability values.	3D ConvNet: average absolute error of 3.37%	3D ConvNets are superior to other ML methods. Accuracy metric does not include ConvNet prediction outliers.
Tembely et al. (2020)	Training: one sandstone and one carbonate	Sandstone: (152 × 152 × 175) 400 samples Carbonate: (100 × 100 × 160) 759 samples	70 to 30%	Different ML methods 3D ConvNet-two convolutional layers	R^2 —coefficient of determination	3D ConvNet: R^2 : 0.85 Physics-informed ConvNet: R^2 : 0.91 (adding porosity and formation factor to the fully connected layer)	Different ML methods are tested. ConvNet has lower accuracy compared to other algorithms, perhaps due to training data-set size.
Tian et al. (2020a)	3D synthetically generated images	4,500 samples	80 to 20%	3D ConvNet: three networks are tested: two to four convolutional layers	R^2 —coefficient of determination RMSE MAE	$R^2 > 0.996$ MAE: 0.017 darcies RMSE: 0.03 darcies	Near-perfect accuracy obtained on synthetic 3D geometries

Table 1—A summary of previous efforts on estimating porous media physical properties using ConvNets. ML = machine learning; MSE = mean squared error.

Research Paper	Type of Data	Training Image Size\Size of Data Set	Training and Testing Split	ConvNet Architecture	Accuracy Metrics	Summary of Reported Accuracy Metrics on the Testing Data Set	Main Findings\Remarks
Tian et al. (2020b)	3D synthetically generated images	1,000 samples	70 to 30%	Genetic algorithm and artificial neural network	R^2 -coefficient of determination	$R^2 > 0.99$ for all different configurations tested	Near-perfect accuracy obtained using synthetic 3D geometries
Wu et al. (2019)	2D synthetically generated images	Three cases: 980 samples, 1,960 samples, 490 samples	3 cases: (98 to 2%) (99 to 1%) (91 to 9%)	2D ConvNet: two convolutional layers	R^2 -coefficient of determination MSE	R^2 : 0.86, 0.87, -0.714 MSE: 0.0008, 0.001076, 0.001553	Adding porosity and surface area to fully connected layer increases performance.

Table 1 (continued)—A summary of previous efforts on estimating porous media physical properties using ConvNets. ML = machine learning; MSE = mean squared error.

In our study, our main contribution focuses on applying a full-scale experimentation through training and testing deeper architectures (compared to previous efforts) for estimating permeability on a diverse data set consisting of (seven sandstone rocks and two carbonate rocks). The range of permeabilities studied in the data sets extends over more than 3 orders of magnitude. To the best of our knowledge, this is the largest data set (with >29 K 3D geometry) presented for training DL models in the DR technology literature. The training experiments use 3D versions of ResNets (He et al. 2016) and ResNext (Xie et al. 2017) to estimate the geometry of porous media for flow-based characterization. The target permeability of 3D porous media is computed through a geometrical finite volume solver (Chung et al. 2019). We tested several variants of ResNet and ResNext with different depths to study the performance gains from deeper networks. We also used conductivity maps instead of binary images as an input to represent the pore space for training where we anticipate performance gains. We statically compare the obtained result through four different regression metrics, including mean relative error. We test the performance of the trained models with an unseen testing sandstone, in which the results are shown to generalize well overall. Finally, we train the best performing model on a carbonate data set, in which the results are shown to be in a similar ballpark to the sandstone data set.

Materials and Image Processing

Two data sets for training are used. The sandstone data set comprises six different sandstone images. The details of all images are shown in **Table 2**. A slightly smaller data set is created for estimation of permeability of carbonates shown in **Table 3**.

Name	Resolution (μm)	Porosity	Size*	Downsampling Factor	Number of Subvolumes	References/ Imaging Facility
Bentheimer sandstone	4.9	0.24	$891 \times 891 \times 1,440$	$2\times$	3,240	Herring et al. (2018)
Berea sandstone	4.6	0.18	$925 \times 925 \times 1,200$	$2\times$	2,160	
Leopard sandstone	3.5	0.14	$1,265 \times 1,265 \times 1,800$	$3\times$	1,836	
Navajo sandstone	1.7	0.14	$1,265 \times 1,265 \times 1,800$	$3\times$	4,800	Argonne National Laboratory
Brown sandstone	1.7	0.13	$891 \times 891 \times 2,000$	$3\times$	3,648	
Gildehauser sandstone	4.4	0.20	$893 \times 897 \times 566$	$3\times$	240	
Doddington sandstone**	2.7	0.20	$1,000 \times 1,000 \times 1,000$	$5\times$	124	Imperial College London
Total					16,048	

*The size of the sandstone images shown is before cropping and downsampling in the x, y, and z dimensions.

**Doddington sandstone is only used for testing the models.

Table 2—Sandstone samples used in the sandstone data set.

Name	Resolution (μm)	Porosity	Size*	Downsampling Factor	Number of Subvolumes	References/ Imaging Facility
Indiana limestone	5.3	0.10	$650 \times 650 \times 1,480$	$2\times$	7,995	University of New
Middle Eastern carbonate	5.3	0.23	$1,212 \times 1,212 \times 1,800$	$2\times$	5,762	South Wales-Tyree X-ray
Total					13,721	

*The size of the carbonate images shown is before cropping and downsampling in the x, y, and z dimensions.

Table 3—Carbonate samples used to create the carbonate data set.

DL models trained using 3D images are constrained by the RAM of the graphics processing unit (GPU) available for training, which is mainly dictated by the model size (how many parameters) and the input image size. The computational and memory requirement of 3D network architectures grow cubically with input resolution/domain size (Riegler et al. 2017). For example, training with domain sizes of 64^3 , 128^3 , and 256^3 would theoretically require 5, 18, and 80 Gigabytes of RAM for a given model size. Thus, training considerably deep networks with volumes bigger than 100^3 exceeds most current GPU memory specifications. Volumetric image sizes less than 100^3 have been reported in porous media literature to train 3D deep networks (Sudakov et al. 2019; Santos et al. 2020; Wang et al. 2020).

To overcome limitations imposed by the GPU memory and maximize the field of view for the input images, we downsample our images so they can fit in the GPU memory. All input images are downsampled by a factor N in a tolerant way that has the minimal effect on the computed permeability and the geometry of the image. In Fig. 1, a 2D image of Berea sandstone before and after downsampling is shown. This downsampling factor is determined based on the number of pore voxels representing local pore space. So, the pore size distribution of original images is computed based on the local pore diameter (Fig. 2). The downsampling replaces resolved pore space greater than N by at least one voxel in the downsampled image. We choose N to preserve at least 95% of the pore space (the area under the curve shown in Fig. 2).

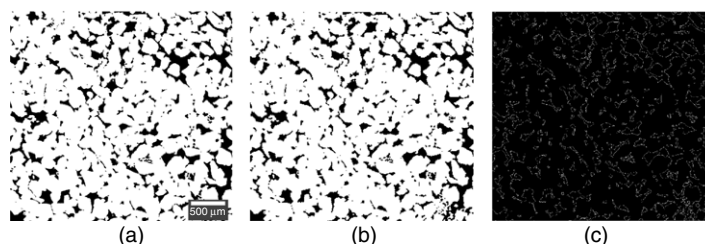


Fig. 1—(a) Slices of the Berea sandstone before downsampling of size (634, 634) and (b) after downsampling of size (317, 317) downsampled by a factor of 2. Grains are in white, and the pore space is in black. (c) Difference image between (a) and (b), showing slight differences at the solid-pore boundaries with no major connectivity loss [(b) is resampled to the original size of (a) for this comparison].

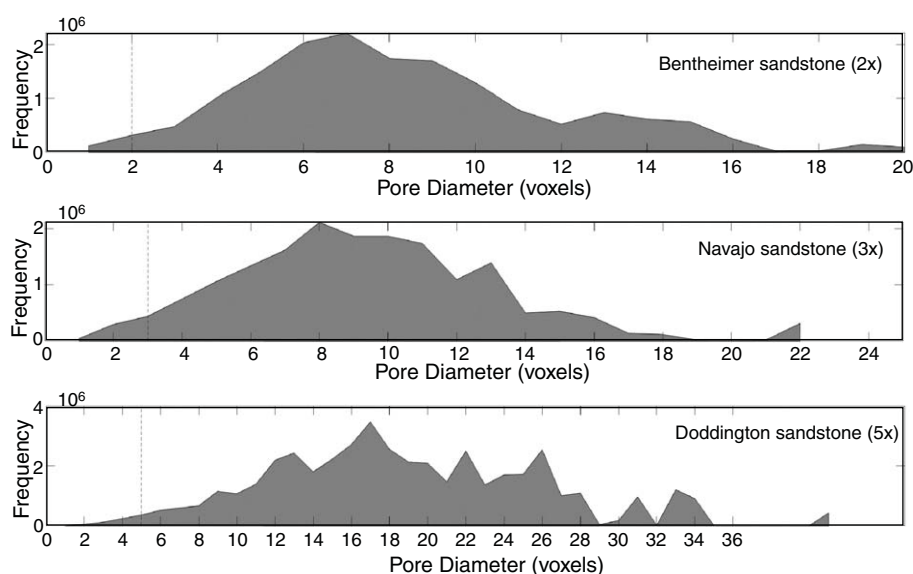


Fig. 2—Local pore size diameter (voxels) is computed to decide a downsampling factor that has minimum effect on the resampled image. The downsampled image must have more than (> 95%) of the original pore space preserved.

The images are downsampled by a factor of N through subdividing the original image of grid size (X, Y, Z) into image size $(\frac{X}{N}, \frac{Y}{N}, \frac{Z}{N})$ by assigning the coarser grid cells the statistical “mode” of the occupying phases in each grid cell size (N^3). To ensure the downsampling has minimal effect on permeability values, the permeability before and after downsampling is measured for all samples, and the difference is found to be less than 2%. After downsampling, all the models are trained with intersecting subvolumes of size 64^3 voxels with a shift of 32 voxels as the striding distance.

Methods

Permeability Computation. The permeability of all samples is computed using the pore-scale finite volume solver (PFVS; Chung et al. 2019). This method relates pore voxels conductivity to the permeability computed from an image. A conductivity value is assigned to each pore voxel based on the distance of the pore voxel from the wall and the size of the local flow channel to which the pore voxel belongs. An illustration of a conductivity map (represented as a d_{\max} domain using Eq. 1) computed for a subvolume of Doddington sandstone is shown in Fig. 3.

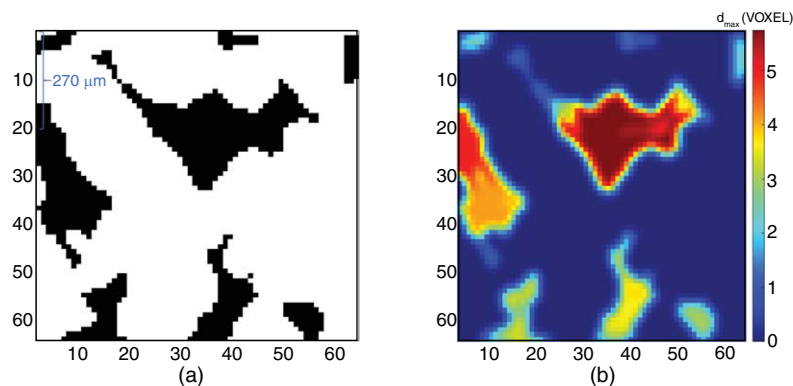


Fig. 3—(a) Slice of a binary subvolume of Doddington sandstone of size 64^3 and (b) the d_{\max} domain (see Eq. 1) of the same image. Warmer regions of d_{\max} correlate with higher voxel conductivity. Both subvolumes are used for training the models in separate experiments. Image axes show the number of voxels.

The conductivity is computed using a weighing function that represents the conductivity of the pore voxel based on its distance from the solid wall and the size of a local flow channel to which the pore voxel belongs (Chung et al. 2019, 2020; Wang et al. 2019c):

$$w = \frac{R^2}{8u} (2d_{\max}d - d^2), \quad \dots \dots \dots (1)$$

where R is the resolution of the image per voxel size (m), u is fluid viscosity (Pa·s), d denotes the digital equivalent of radial distance from the inner wall (voxel), and d_{\max} is the digital equivalent of the maximum inscribed radius of the local channel (voxel). To obtain the local conductivity of the pore voxels, the Euclidean distance transform of the segmented image is portioned based on the maximum radius of the local flow channel. The algorithm for computing d and d_{\max} is described in detail in Chung et al. (2019).

PFVS has been tested against the Stokes solver in various rock samples. The permeabilities estimated are within 11% compared to the permeability obtained using the Stokes solver (Chung et al. 2019). However, PFVS is chosen over classic simulation methods because of its computational efficiency because a large number of simulations are required to train ConvNets (Wang et al. 2019c). The PFVS computation time that scales with the domain size can be described by power-law relationship with an exponent of 1.16 (or 80% lower compared to the Stokes solver).

For permeability computations, we assume a unified voxel resolution of 4 μm for all geometries. The permeability can be rescaled/computed with desired resolution if the spatial resolution for a given geometry of porous media is known using Eq. 2.

$$K_{\text{Actual}} = \left(\frac{R_{\text{Actual}}^2}{R_{\text{Network}}^2} \right) \times K_{\text{Network}}, \quad \dots \dots \dots (2)$$

where K_{Actual} and K_{Network} are the actual and network estimation permeabilities. R_{Actual} and R_{Network} are the actual image resolution and the assumed imaged resolution. During simulations, we obtain both the permeability value and the conductivity of pore voxels as a 3D map of each subvolume. We train the models separately using the binary images and the conductivity maps shown in Fig. 3. Based on the preliminary training experiments, we find the minimal preprocessing step of removing all unconnected pore voxels not contributing to the flow before training improve network convergence and accelerate the learning process. We augment our data set by computing the permeability in the X , Y , and Z directions, which increases the data-set size by a factor of 3.

Networks Architecture. In this study, a special architecture of ConvNets called deep ResNets (proposed by He et al. 2016) is trained for permeability estimation. ResNet and its variants have been used for various image-related problems, such as image segmentation and classification and object detection, to mention a few (Zhang et al. 2017; Wu et al. 2019). They have been the core architectures for the best performing models on large data sets such as ImageNet (Deng et al. 2009) because of their powerful feature representation ability. ResNets incorporate blocks of skip (or residual) connections between some nonsucceeding layers (compare with Fig. 4). This copies the signal at the arbitrary layer and passes it “as is” toward the following block. Residual blocks improve training dynamics in the model and efficiently estimate very deep models (i.e., dozens of layers).

The network architectures used in this study are similar to the ones described in Hara et al. (2018) for action recognition in videos, except we modify it to use with volumetric images as inputs. In this work, we are also concerned with regression tasks, thus using the linear output layer. The configuration of the residual blocks for the architectures used in this work are shown in Fig. 4. In Table 4, we show the full network architectures for regression. We opt to experiment the performance of different architectures and depths because the literature on regression networks is not vast compared to other tasks such as classification. Hence, the accuracy gains of using a deeper network can be quantified.

The basic ResNet block contains two convolutional layers each, followed by batch normalization and a rectified linear unit (ReLU). The signature skip connections of ResNets connect the top of the basic block to just before the ReLU. Skip connections of Type A described in He et al. (2016) are used in basic blocks. The bottleneck block design has three convolutional layers followed by batch normalization and ReLU. Identity connections in bottleneck architecture are all of Type A, except where the dimensions of the tensors are changed (see Table 4), where we use Type B skip connections (He et al. 2016). The main difference between the two block designs is the efficiency of computation. The bottleneck design is more economical when building deeper networks as reported when these designs were trained using different data sets (He et al. 2016).

Training Settings, System Specification, Hyperparameters, and Metrics. This section describes the training and evaluation protocol, experimental settings, the choice of hyperparameters for training the networks, and the metrics used to evaluate the models. Table 5 reports the hyperparameters used to train each network variant.

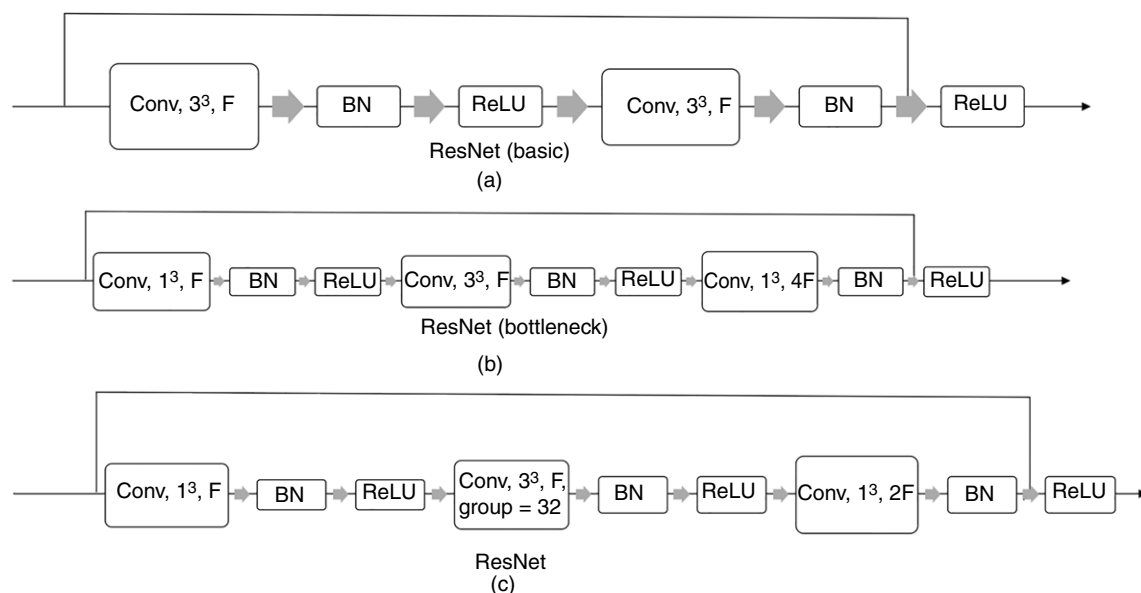


Fig. 4—Residual blocks of architectures: (a) ResNet (basic), (b) ResNet (bottleneck), and (c) ResNext. (Conv, k^3 , F) refers to the kernel size k , and the number of feature maps F of the convolution operation (this is provided in Table 4), (group) refers to the number of groups of convolutions or (cardinality) as described in the original paper (Xie et al. 2017). BN refers to batch normalization (Ioffe and Szegedy 2015), and ReLU refers to the rectified linear unit activation (Nair and Hinton 2010).

Model	Block Type	ResNet-34 Basic	ResNet- [50,101,152] Bottleneck	ResNeXt-50 ResNext
Conv_1		conv, $k = 7 \times 7 \times 7$, $F = 64$, stride = 1		
Conv_2	F^*	64	64	64
	N^{**}	3	3	3
Conv_3	F	128	128	128
	N	4	[4,4,8]	4
Conv_4	F	256	256	256
	N	6	[6,23,36]	6
Conv_5	F	512	512	512
	N	3	3	3
Average pooling		Global average pooling		
Top layers		FC layer-1 (1024), FC layer-2 (1)		

* F corresponds to the number of feature maps in the residual block as shown in Fig. 4.

** N is the number of blocks for a given layer.

Table 4—Network architectures. Max-pooling with a kernel size of $3 \times 3 \times 3$ and stride of 2 before Conv_2 is applied for downsampling. Every layer (Conv_x) is followed by batch normalization (Ioffe and Szegedy 2015) and ReLU activation (Nair and Hinton 2010). Spatial downsampling is applied at layers (Conv_3, Conv_4, and Conv_5) with a stride of 2.

Hyperparameter	ResNet [34,50,101,152]	ResNext-50
Batch size	[8,8,6,4]	8
Optimizer	Adam (Kingma and Ba 2015)	
Learning rate	1×10^{-5}	
Weight decay	1×10^{-4}	
Loss function	MAE	

Table 5—Hyperparameters settings for training the models.

We train all the models using a DL Pytorch (Paszke et al. 2019) toolkit using a single RTX 2080 Nvidia GPU. This GPU has 8 Gigabytes of RAM, installed on a PC with an Intel i7-8700 (a 3.20 GHz with six cores) CPU processor and 64 Gigabytes DDR4 RAM.

Early stopping of training with a patience of 15 epochs (when the validation error does not improve for 15 epochs) is applied to avoid overfitting (Caruana et al. 2001). The weights of the models are saved whenever the validation error decreases. Our training/validation/testing splits of the data sets are 70/15/15%, respectively, not including the Doddington sandstone samples. The validation

data set is used as a separate subset to assess the network performance while training for tuning hyperparameters (e.g., learning rate and weight decay).

During training, we monitor four metrics to assess the model accuracy: EVS, MAE, mean squared error (MSE), and mean absolute relative error (MARE). MAE and MSE are very common criteria for regression problem monitoring and detecting outliers (Botchkarev 2018). EVS is a statistical measure that estimates the proportion of which a model accounts for variation of a given data set. Possible score for EVS is 1.0; lower values correspond to worse performance. Mean relative error estimates the average relative error to the ground truth values for all samples. In **Table 6**, we show the mathematical formula for computing each metric. We use A_j for the actual value of the j th sample, P for the predicted value, Var for the variance, and n for the number of samples in each data set.

Metric	Metric Formula
EVS	$1 - \frac{\text{Var}(A_j - P_j)}{\text{Var}(A_j)}$
MAE	$\frac{1}{n} \sum_{j=1}^n (A_j - P_j) $
MSE	$\frac{1}{n} \sum_{j=1}^n (A_j - P_j)^2$
MARE	$\frac{1}{n} \sum_{j=1}^n \frac{ (A_j - P_j) }{A_j}$

Table 6—Metrics for assessing the accuracy of regression.

Results and Discussion

Binary Images and Conductivity Maps Comparison. We compare the use of binary/segmented images as an input for training against the use of conductivity maps. It is noticed that training with conductivity maps generally yields better performance when benchmarking against two ResNet architectures: ResNet-34 and ResNet-50. The aforementioned evaluation metrics are monitored on a separate validation set during the training experiments and are shown in **Fig. 5**. This behavior is expected because the conductivity maps contain a richer representation of what determines permeability, where not only the morphology is defined, but also the pore voxel connectivities are cast for better permeability estimation. We base all further model experiments in the remainder of the study on the conductivity maps as the input images for training.

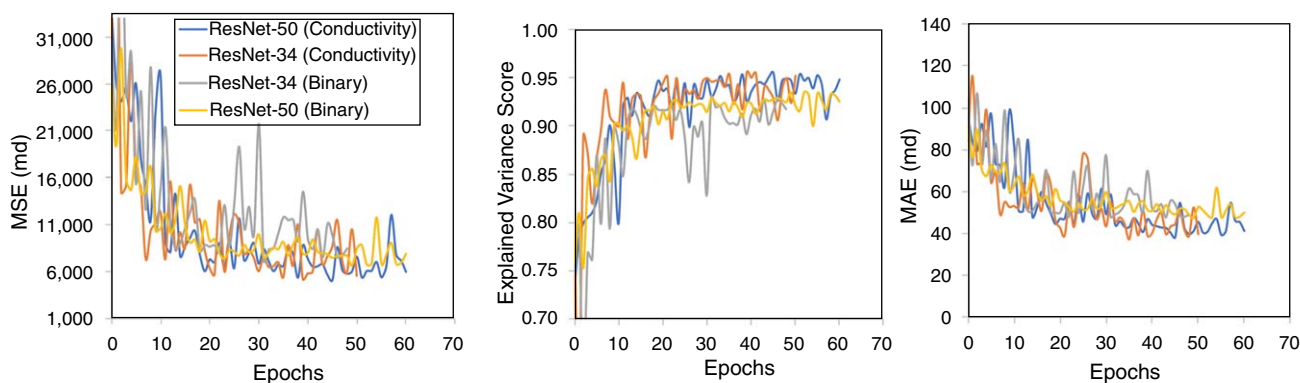


Fig. 5—Comparison of the performance of ResNet-34 and ResNet-50 when using binary images against conductivity maps.

Regression Experiments Using ResNet Variants. In this section, we test several ResNet variants for flow estimation. The training settings for all the experiments are shared and reported in Tables 4 and 5. Only the model architecture is changed for each run. The regression evaluation metrics for the best model performance using the testing set are reported in **Table 7**. The models achieve very similar performances overall. There are slight gains in accuracy when increasing the depth of the network; however, this is at the expected cost of higher computation requirements (longer training time). In **Fig. 6**, the training loss is plotted against the number of epochs. The figure shows the convergence in a deeper network is slower, requiring training for more epochs.

Model	MSE (md)	EVS	MAE (md)	MARE (%)	Training Duration (hours)
ResNet-34	5012.9	0.953	25.94	34	11
ResNet-50	4765.62	0.961	28.82	28	17
ResNet-101	4811.55	0.963	28.23	28	36
ResNet-152	4792.23	0.964	25.88	25	86
ResNext-50	6992.23	0.943	34.27	34	26

Table 7—ResNet performance on the testing set. Bold results show the best values of each metric obtained during training.

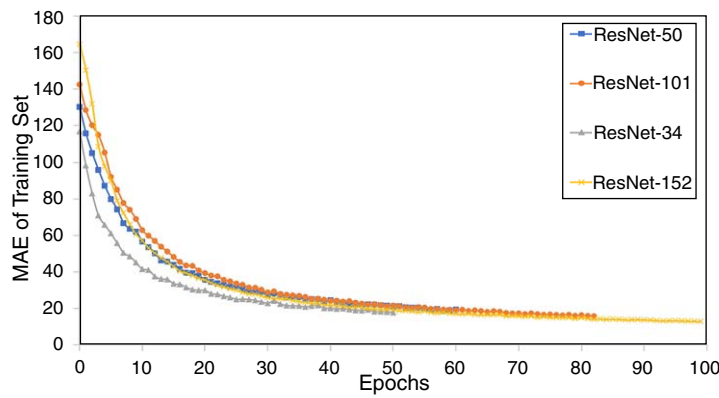


Fig. 6—Training loss (MAE) plotted against the number of training epochs.

The actual permeabilities as obtained with numerical simulation are plotted against the ResNet-50 estimation in Fig. 7. The data sets considered in this study are not equally distributed across the full range of permeabilities but rather skewed to values closer to zero. The existence of a few prediction outliers with relative error exceeding 50% is apparent in some samples. The anticipation of outliers in neural network regressions has been reported in literature for different regression problems such as age estimation (Lathuilière et al. 2018; Rothe et al. 2018), and several methods have been suggested to mitigate it such as the use of robust regression methods (Belagiannis et al. 2015; Lathuilière et al. 2018). Yet, applying such methods lies beyond the scope of this study. The mean relative error of the best performing model is 25%, in which the highest 10th percentile of relative errors is for samples less than 100 md of permeability. These errors possibly arise from the complex geometries with narrow pathways that the network mispredict. Also, this is a side effect of using L1 loss, which might not be sensitive to relative error considering the backpropagation through which the network weights are updated.

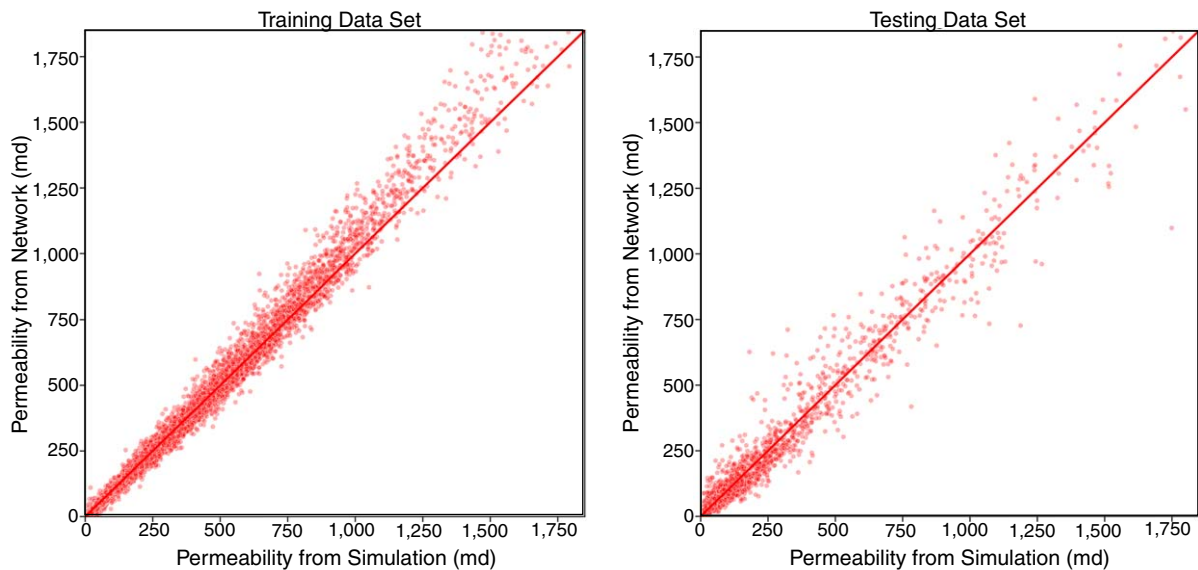


Fig. 7—Permeability values from simulation are plotted against the permeability using the network estimation. The determination coefficient R^2 of the training data set (left) is 0.984, and the testing data set (right) is 0.956. The red line shows the line equation $y = x$.

Testing with Unseen Sandstone Samples. All testing subvolumes in the previous sections are unseen and have not been used in training but part of the samples was used in training. In this section, the models were tested using a holdout Doddington sandstone that has not been included in the training data set. In total, 124 subvolumes were tested using the best models' weights (according to validation performance) as obtained during training. Table 8 shows the performance metrics of each model. The models' performances are in a similar ballpark as the results reported on the in-domain testing set with ResNet-152 characterized by a best performance. Fig. 8 shows the permeability from simulation plotted against ResNet-152 predictions. The EVS is 0.87, slightly lower (less than 10%) than the average of the testing set. However, the computed prediction errors using MAE and MSE metrics are 18.92 and 3072 md, respectively, which are lower compared to the experiments run on the testing set by 30%. The MARE for the best model, ResNet-152, is 18.9%. This reported relative error is not high if compared to indirect pore-scale modeling techniques to compute permeability, such as pore network modeling or Laplace solvers (Dong and Blunt 2009; Arns and Adler 2018; Baychev et al. 2019). The reported errors in these studies are generally higher than 20%. Also, the inconsistencies between various numerical solvers (such as the finite volume method) compared to classic Lattice Boltzmann methods and Stokes solvers have similar relative errors (Yang et al. 2016; Gerke et al. 2018). The inference time of deep models per sample is four times less than that required to run the simulation used for the same domain size. So, the error trade-off with speed can be more justified.

Model	MSE (md)	EVS	MAE (md)	MARE (%)	Inference Time per Sample (ms)
ResNet-34	3244	0.87	44.3	21.3	61
ResNet-50	3206	0.87	41.8	21.8	70
ResNet-101	3638	0.86	42.5	22	88
ResNet-152	3072	0.87	39.10	18.9	105
ResNext-50	4172	0.83	51.02	25.4	56

Table 8—Models performance tested using an external sandstone. Bold results show the best values of each metric.

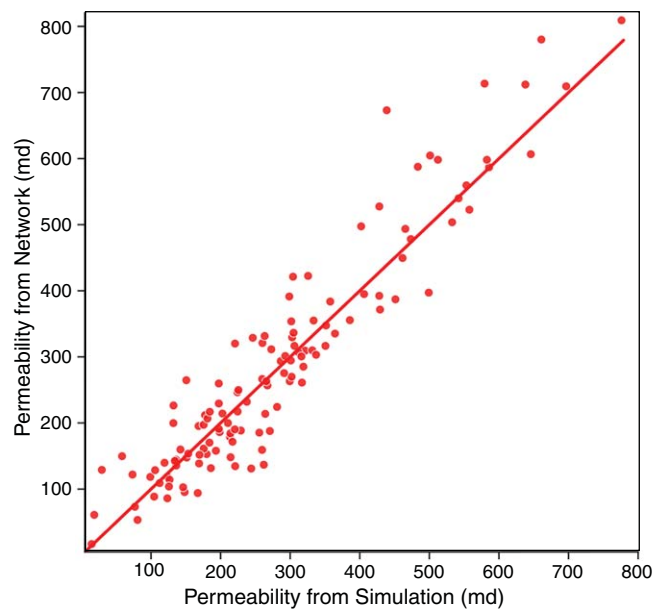


Fig. 8—Permeability of subvolumes of an unseen sandstone plotted against the ResNet-152 predictions. Determination coefficient R^2 is 0.86. The red line is the line equation $y = x$.

Training and Testing on Carbonate Samples. The regression experiment using model ResNet-152 is repeated using the carbonate data set in which carbonate images are used for training. The results are shown in Fig. 9. Table 9 shows the performance metrics on the testing set in which the metrics overall show a similar trend to the results obtained when training using sandstone. However, it was noticed again that the highest top 10th percentile of relative error is from samples with relatively low permeability (< 500 md). The reason is perhaps the complexity of the pore-space geometry and the limited connectivity between pore bodies where the network mis-estimates such bottlenecks. Model regularization and incorporating robust regression techniques for outliers detection should have a significant improvement on such models, which is an active research area (Diskin et al. 2017; Lathuilière et al. 2018).

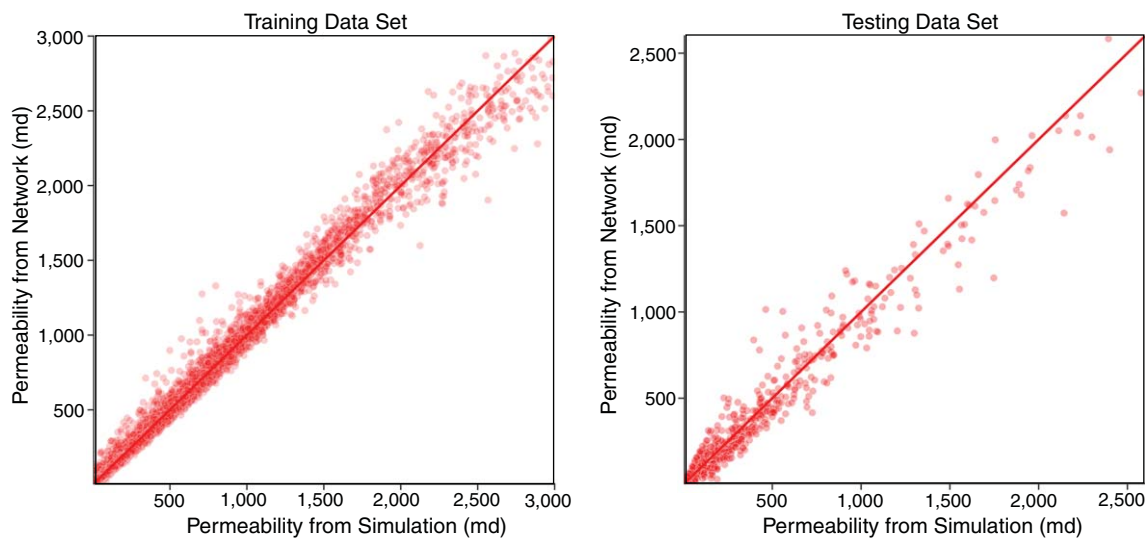


Fig. 9—Permeability of carbonate subvolumes plotted against ResNet-152 predictions. Determination coefficients R^2 are 0.98 for training and 0.95 for testing. The red line is the line equation $y = x$.

Model	MSE (md)	EVS	MAE (md)	MARE (%)
ResNet-152	10 693	0.95	66.5	26.8

Table 9—Performance metrics obtained from the testing set when training model ResNet-152 on the carbonate data set.

The results and error margins when training with more complex geometries of carbonates are comparable with the previous experiments on sandstones. This shows the capacity of ResNets as models, and their ability to learn complex features considering the different porosity ranges and geometrical features of carbonates. This is another significant advantage over indirect pore-scale modeling in which the performance in general declines with the geometry complexity (Dong and Blunt 2009; Arns and Adler 2018).

Because the introduction of GPUs facilitated training deeper networks, such as the ones presented in this study, computational efficiency remains an important aspect for achieving optimal accuracy. The gains in accuracy through training deeper neural networks may not be significant, considering the training time. ResNet-50 and ResNet-152 achieve very close margins of accuracy with a considerably longer training time for the latter. However, considering the inference time for all models taking less than a second and the fact that training is only done once, the gain in accuracy with respect to training time can be justified. The rapid growth of computational resources (i.e., GPU computational capacity and using multiple GPUs for training) should boost the robustness and generalization of DL models, larger data sets, domain sizes, and deeper models, boosting the robustness and the generalization capacity of deep regression models.

Conclusions

Applying deep neural networks for estimation of permeability based on 3D images of rocks as an input has shown to produce a comparable result to the values obtained via numerical simulations. Several 3D variants of deep ResNets are trained to estimate the permeability of subvolumes of size 64^3 voxels extracted from larger downsampled volumes. Two data sets are generated from sandstone and carbonate images with a total number of images exceeding 29 K subvolume for training and testing. The training experiments are conducted using two forms of inputs: binary images and conductivity maps (where pore voxels are assigned a conductivity value based on Euclidean distance from the closest grain boundaries). Several conclusions have been made from the training experiments. First, training with a richer representation of pore space yields considerably better estimation results. Conductivity maps boost the network performance in estimating the permeability compared to binary images, decreasing the MAE metric by 37.5%. Second, network depth can improve regression accuracy considerably. When the ResNet variants are compared, deeper networks performed better compared to shallower ones, at the cost of higher computational cost, for example, ResNet-152 decreases the MAE metric by 10% compared to ResNet-50. The evaluation metrics of the best performing model, ResNet-152, are MAE of 25.88 md, EVS of 0.964, and MARE of 25%. The most promising model was also tested using an unseen Doddington sandstone. The evaluation metrics show a similar trend to results obtained from the original testing set with MAE of 18.92 md, EVS of 0.87, and MARE of 18.9% for ResNet-152. Finally, the results obtained when training ResNet-152 on more heterogeneous and complex geometries of carbonate images are very similar with MARE of 26.8% and MAE of 66.8 md. This shows the capacity of DL models to learn more complex geometries without an obvious implication on the estimation accuracy if compared with more classical methods of estimating permeability.

This study serves as a first step toward obtaining a fully automated framework for estimating physical properties from the pore space geometry for which we consider 64^3 subvolumes of various DRs for training. The advancement of computational technology (especially GPUs) will enable training with larger domains and data-set sizes. The focus of future studies will include training with more complex geometries of porous media including fractured media. We also look forward to enhancing the generalization ability of models through combining robust regression methods alongside neural networks and employing ensemble learning.

Nomenclature

d	= digital equivalent of the radial distance from the inner wall, voxels
d_{\max}	= digital equivalent of the largest inscribed radius, voxels
K_{actual}	= absolute permeability from numerical simulation, L^2
K_{Network}	= absolute permeability from Network estimation, L^2
N	= downsampling factor, dimensionless
R	= resolution, L
w	= local voxel conductivity, $LM^{-1}T$
μ	= fluid viscosity, MLT^{-2}

Acknowledgments

Naif Alqahtani acknowledges the graduate fellowship provided by Saudi Aramco. We acknowledge the Tyree X-ray imaging facility personnel for conducting the required imaging for this study.

References

- Al-Kharusi, A. S. and Blunt, M. J. 2007. Network Extraction from Sandstone and Carbonate Pore Space Images. *J Pet Sci Eng* **56** (4): 219–231. <https://doi.org/10.1016/j.petrol.2006.09.003>.
- Alqahtani, N., Alzubaidi, F., Armstrong, R. T. et al. 2020. Machine Learning for Predicting Properties of Porous Media from 2d X-Ray Images. *J Pet Sci Eng* **184**: 106514. <https://doi.org/10.1016/j.petrol.2019.106514>.
- Alqahtani, N., Armstrong, R. T., and Mostaghimi, P. 2018. Deep Learning Convolutional Neural Networks to Predict Porous Media Properties. Paper presented at the SPE Asia Pacific Oil and Gas Conference and Exhibition, Brisbane, Australia, 23–25 October. SPE-191906-MS. <https://doi.org/10.2118/191906-MS>.
- Ar Rushood, I., Alqahtani, N., Wang, Y. D. et al. 2020. Segmentation of X-Ray Images of Rocks Using Deep Learning. Paper presented at the SPE Annual Technical Conference and Exhibition, Virtual, 26–29 October. SPE-201282-MS. <https://doi.org/10.2118/201282-MS>.
- Arns, C. H., Knackstedt, M. A., Pinczewski, V. W. et al. 2004. Virtual Permeametry on Microtomographic Images. *J Pet Sci Eng* **45** (1–2): 41–46. <https://doi.org/10.1016/j.petrol.2004.05.001>.

- Arns, C. H. and Adler, P. M. 2018. Fast Laplace Solver Approach to Pore-Scale Permeability. *Phys Rev E* **97** (2): 023303. <https://doi.org/10.1103/PhysRevE.97.023303>.
- Baychev, T. G., Jivkov, A. P., Rabbani, A. et al. 2019. Reliability of Algorithms Interpreting Topological and Geometric Properties of Porous Media for Pore Network Modelling. *Transp Porous Media* **128** (1): 271–301. <https://doi.org/10.1007/s11242-019-01244-8>.
- Bear, J. 1972. *Dynamics of Fluids in Porous Media*. Mineola, New York, USA: Dover Publications.
- Belagiannis, V., Ruppelrecht, C., Carneiro, G. et al. 2015. Robust Optimization for Deep Regression. Paper presented at the IEEE International Conference on Computer Vision, Santiago, Chile, 13–16 December. <https://doi.org/10.1109/ICCV.2015.324>.
- Bhatnagar, P. L., Gross, E. P., and Krook, M. 1954. A Model for Collision Processes in Gases. I. Small Amplitude Processes in Charged and Neutral One-Component Systems. *Phys Rev* **94** (3): 511–525. <https://doi.org/10.1103/PhysRev.94.511>.
- Blunt, M. J., Bijeljic, B., Dong, H. et al. 2013. Pore-Scale Imaging and Modelling. *Adv Water Resour* **51**: 197–216. <https://doi.org/10.1016/j.advwatres.2012.03.003>.
- Botchkarev, A. 2018. Performance Metrics (Error Measures) in Machine Learning Regression, Forecasting and Prognostics: Properties and Typology. *Interdiscip J Inf* **14**: 45–79. <https://doi.org/10.28945/4184>.
- Carman, P. C. 1956. *Flow of Gases through Porous Media*. Waltham, Massachusetts, USA: Academic Press Inc.
- Caruana, R., Lawrence, S., and Giles, C. L. 2001. Overfitting in Neural Nets: Backpropagation, Conjugate Gradient, and Early Stopping. *Adv Neural Inf Process Syst* **13**: 402–408.
- Chung, T., Wang, Y. D., Armstrong, R. T. et al. 2019. Approximating Permeability of Microcomputed-Tomography Images Using Elliptic Flow Equations. *SPE J* **24** (3): 1154–1163. SPE-191379-PA. <https://doi.org/10.2118/191379-PA>.
- Chung, T., Wang, Y. D., Armstrong, R. T. et al. 2020. Voxel Agglomeration for Accelerated Estimation of Permeability from Micro-CT Images. *J Pet Sci Eng* **184**: 106577. <https://doi.org/10.1016/j.petrol.2019.106577>.
- Coenen, J., Tchouparova, E., and Jing, X. 2004. Measurement Parameters and Resolution Aspects of Micro X-Ray Tomography for Advanced Core Analysis. Paper presented at the International Symposium of the Society of Core Analysts, Abu Dhabi, UAE, 5–9 October. SCA2004-36.
- Deng, J., Dong, W., Socher, R. et al. 2009. ImageNet: A Large-Scale Hierarchical Image Database. *Proc.*, IEEE Conference on Computer Vision and Pattern Recognition, Miami, Florida, USA, 248–255. <https://doi.org/10.1109/CVPR.2009.5206848>.
- Diskin, T., Draskovic, G., Pascal, F. et al. 2017. Deep Robust Regression. Paper presented at the IEEE 7th International Workshop on Computational Advances in Multi-Sensor Adaptive Processing (CAMSAP), Curacao, 10–13 December. <https://doi.org/10.1109/CAMSAP.2017.8313200>.
- Dong, H. and Blunt, M. J. 2009. Pore-Network Extraction from Micro-Computerized-Tomography Images. *Physical Review E* **80** (3): 036307.
- Ferréol, B. and Rothman, D. H. 1995. Lattice-Boltzmann Simulations of Flow through Fontainebleau Sandstone. *Transp Porous Media* **20** (1–2): 3–20. <https://doi.org/10.1103/PhysRevE.80.036307>.
- Fredrich, J. T., DiGiovanni, A. A., and Noble, D. R. 2006. Predicting Macroscopic Transport Properties Using Microscopic Image Data. *J Geophys Res Solid Earth* **111** (B3): 1–14. <https://doi.org/10.1029/2005JB003774>.
- Gerke, K. M., Vasilyev, R. V., Khirevich, S. et al. 2018. Finite-Difference Method Stokes Solver (FDMSS) for 3D Pore Geometries: Software Development, Validation and Case Studies. *Computational Geosciences* **114**: 41–58. <https://doi.org/10.1016/j.cageo.2018.01.005>.
- Girshick, R., Donahue, J., Darrell, T. et al. 2014. Rich Feature Hierarchies for Accurate Object Detection and Semantic Segmentation. Paper presented at the IEEE Conference on Computer Vision and Pattern Recognition, Columbus, Ohio, USA, 24–27 June. <https://doi.org/10.1109/CVPR.2014.81>.
- Goodfellow, I., Bengio, Y., and Courville, A. 2016. *Deep Learning*. Cambridge, Massachusetts, USA: MIT Press.
- Hara, K., Kataoka, H., and Satoh, Y. 2018. Can Spatiotemporal 3D CNNs Retrace the History of 2D CNNs and ImageNet? Paper presented at the IEEE/CVF Conference on Computer Vision and Pattern Recognition, Salt Lake City, Utah, USA, 18–23 June. <https://doi.org/10.1109/CVPR.2018.00685>.
- He, K., Zhang, X., Ren, S. et al. 2016. Deep Residual Learning for Image Recognition. Paper presented at the IEEE Conference on Computer Vision and Pattern Recognition (CVPR), Las Vegas, Nevada, USA, 26 June–1 July. <https://doi.org/10.1109/CVPR.2016.90>.
- Herring, A., Sheppard, A., Turner, M. et al. 2018. Multiphase Flows in Sandstones. <https://doi.org/10.17612/P7MH3M>.
- Hong, J. and Liu, J. 2020. Rapid Estimation of Permeability from Digital Rock Using 3D Convolutional Neural Network. *Computational Geosciences* **24** (4): 1523–1539. <https://doi.org/10.1007/s10596-020-09941-w>.
- Ioffe, S. and Szegedy, C. 2015. Batch Normalization: Accelerating Deep Network Training by Reducing Internal Covariate Shift. In *Proceedings of the 32nd International Conference on Machine Learning*, Vol. 37, 448–456. <http://proceedings.mlr.press/v37/ioffe15.html>.
- Jin, G., Patzek, T. W., and Silin, D. B. 2004. Direct Prediction of the Absolute Permeability of Unconsolidated and Consolidated Reservoir Rock. Paper presented at the SPE Annual Technical Conference and Exhibition, Houston, Texas, USA, 26–29 September. SPE-90084-MS. <https://doi.org/10.2118/90084-MS>.
- Kamrava, S., Tahmasebi, P., and Sahimi, M. 2019a. Enhancing Images of Shale Formations by a Hybrid Stochastic and Deep Learning Algorithm. *Neural Networks* **118**: 310–320. <https://doi.org/10.1016/j.neunet.2019.07.009>.
- Kamrava, S., Tahmasebi, P., and Sahimi, M. 2019b. Linking Morphology of Porous Media to Their Macroscopic Permeability by Deep Learning. *Transp Porous Media* **131** (2): 427–448. <https://doi.org/10.1007/s11242-019-01352-5>.
- Karimpouli, S. and Tahmasebi, P. 2019. Segmentation of Digital Rock Images Using Deep Convolutional Autoencoder Networks. *Computational Geosciences* **126**: 142–150. <https://doi.org/10.1016/j.cageo.2019.02.003>.
- Katz, A. J. and Thompson, A. H. 1986. Quantitative Prediction of Permeability in Porous Rock. *Phys Rev B* **34** (11): 8179–8181. <https://doi.org/10.1103/PhysRevB.34.8179>.
- Kingma, D. P. and Ba, J. 2015. Adam: A Method for Stochastic Optimization. <https://arxiv.org/abs/1412.6980>.
- Krizhevsky, A., Sutskever, I., and Hinton, G. E. 2012. ImageNet Classification with Deep Convolutional Neural Networks. *Commun ACM* **60** (6): 84–90. <https://doi.org/10.1145/3065386>.
- Lathuilière, S., Mesejo, P., Alameda-Pineda, X. et al. 2018. Deepgum: Learning Deep Robust Regression with a Gaussian-Uniform Mixture Model. Paper presented at the ECCV 2018—European Conference on Computer Vision, Munich, Germany, 8–14 September. https://doi.org/10.1007/978-3-030-01228-1_13.
- Lathuilière, S., Mesejo, P., Alameda-Pineda, X. et al. 2019. A Comprehensive Analysis of Deep Regression. *IEEE Trans Pattern Anal Mach Intell* **42** (9): 2065–2081. <https://doi.org/10.1109/TPAMI.2019.2910523>.
- Lecun, Y., Bottou, L., Bengio, Y. et al. 1998. Gradient-Based Learning Applied to Document Recognition. *Proc IEEE* **86** (11): 2278–2324.
- Lin, G., Shen, C., Van Den Hengel, A. et al. 2016. Efficient Piecewise Training of Deep Structured Models for Semantic Segmentation. Paper presented at the IEEE Conference on Computer Vision and Pattern Recognition, Las Vegas, Nevada, USA, 26 June–1 July. <https://doi.org/10.1109/CVPR.2016.348>.
- Long, J., Shelhamer, E., and Darrell, T. 2015. Fully Convolutional Networks for Semantic Segmentation. Paper presented at the IEEE Conference on Computer Vision and Pattern Recognition (CVPR), Boston, Massachusetts, USA, 7–12 June. <https://doi.org/10.1109/CVPR.2015.7298965>.

- Maturana, D. and Scherer, S. 2015. VoxNet: A 3D Convolutional Neural Network for Real-Time Object Recognition. Paper presented at the IEEE/RSJ International Conference on Intelligent Robots and Systems (IROS), Hamburg, Germany, 28 September–2 October. <https://doi.org/10.1109/IROS.2015.7353481>.
- Mosser, L., Dubrule, O., and Blunt, M. J. 2017. Reconstruction of Three-Dimensional Porous Media Using Generative Adversarial Neural Networks. *Phys Rev E* **96** (4): 043309. <https://doi.org/10.1103/PhysRevE.96.043309>.
- Mostaghimi, P., Armstrong, R. T., Gerami, A. et al. 2017. Cleat-Scale Characterisation of Coal: An Overview. *J Nat Gas Sci Eng* **39**: 143–160. <https://doi.org/10.1016/j.jngse.2017.01.025>.
- Mostaghimi, P., Bijeljic, B., and Blunt, M. 2012. Simulation of Flow and Dispersion on Pore-Space Images. *SPE J.* **17** (4): 1131–1141. SPE-135261-PA. <https://doi.org/10.2118/135261-PA>.
- Mostaghimi, P., Blunt, M. J., and Bijeljic, B. 2013. Computations of Absolute Permeability on Micro-CT Images. *Math Geosci* **45** (1): 103–125. <https://doi.org/10.1007/s11004-012-9431-4>.
- Nair, V. and Hinton, G. E. 2010. Rectified Linear Units Improve Restricted Boltzmann Machines. Paper presented at the 27th International Conference on International Conference on Machine Learning, Haifa, Israel, 21–24 June.
- Niu, Y., Mostaghimi, P., Shabaninejad, M. et al. 2020a. Digital Rock Segmentation for Petrophysical Analysis with Reduced User Bias Using Convolutional Neural Networks. *Water Resour Res* **56** (2): e2019WR026597. <https://doi.org/10.1029/2019WR026597>.
- Niu, Y., Wang, Y. D., Mostaghimi, P. et al. 2020b. An Innovative Application of Generative Adversarial Networks for Physically Accurate Rock Images with an Unprecedented Field of View. *Geophys Res Lett* **47** (23): e2020GL089029. <https://doi.org/10.1029/2020GL089029>.
- Pan, C., Hilpert, M., and Miller, C. T. 2001. Pore-Scale Modeling of Saturated Permeabilities in Random Sphere Packings. *Phys Rev E* **64** (6): 066702. <https://doi.org/10.1103/PhysRevE.64.066702>.
- Paszke, A., Gross, S., Chintala, S. et al. 2017. Automatic Differentiation in Pytorch. Paper presented at the 31st Conference on Neural Information Processing Systems (NIPS 2017), Long Beach, California, USA, 4–9 December.
- Riegler, G., Osman Ulusoy, A., and Geiger, A. 2017. Octnet: Learning Deep 3D Representations at High Resolutions. <https://arxiv.org/abs/1611.05009>.
- Rothe, R., Timofte, R., and Van Gool, L. 2018. Deep Expectation of Real and Apparent Age from a Single Image without Facial Landmarks. *Int J Comput Vision* **126** (2–4): 144–157. <https://doi.org/10.1007/s11263-016-0940-3>.
- Sahimi, M. 2011. *Flow and Transport in Porous Media and Fractured Rock: From Classical Methods to Modern Approaches*, second edition, New York City, New York, USA: Wiley.
- Santos, J. E., Xu, D., Jo, H. et al. 2020. PoreFlow-Net: A 3D Convolutional Neural Network to Predict Fluid Flow through Porous Media. *Adv Water Resour* **138**: 103539. <https://doi.org/10.1016/j.advwatres.2020.103539>.
- Sermanet, P., Eigen, D., Zhang, X. et al. 2013. Overfeat: Integrated Recognition, Localization and Detection Using Convolutional Networks. <https://arxiv.org/abs/1312.6229>.
- Silin, D. and Patzek, T. 2006. Pore Space Morphology Analysis Using Maximal Inscribed Spheres. *Physica A: Stat Mech Appl* **371** (2): 336–360. <https://doi.org/10.1016/j.physa.2006.04.048>.
- Simonyan, K. and Zisserman, A. 2014. Very Deep Convolutional Networks for Large-Scale Image Recognition. <http://export.arxiv.org/abs/1409.1556>.
- Sudakov, O., Burnaev, E., and Koroteev, D. 2019. Driving Digital Rock towards Machine Learning: predicting Permeability with Gradient Boosting and Deep Neural Networks. *Comput Geosci* **127**: 91–98. <https://doi.org/10.1016/j.cageo.2019.02.002>.
- Szegedy, C., Liu, W., Jia, Y. et al. 2015. Going Deeper with Convolutions. Paper presented at the IEEE Conference on Computer Vision and Pattern Recognition, Boston, Massachusetts, USA, 7–12 June. <https://doi.org/10.1109/CVPR.2015.7298594>.
- Tahmasebi, P., Kamrava, S., Bai, T. et al. 2020. Machine Learning in Geo- and Environmental Sciences: From Small to Large Scale. *Adv Water Resour* **142**: 103619. <https://doi.org/10.1016/j.advwatres.2020.103619>.
- Tembely, M., AlSumaiti, A. M., and Alameri, W. 2020. A Deep Learning Perspective on Predicting Permeability in Porous Media from Network Modeling to Direct Simulation. *Computational Geosciences* **24** (4): 1541–1556. <https://doi.org/10.1007/s10596-020-09963-4>.
- Tian, J., Qi, C., Sun, Y. et al. 2020a. Surrogate Permeability Modelling of Low-Permeable Rocks Using Convolutional Neural Networks. *Computer Methods in Applied Mechanics and Engineering* **366**: 113103. <https://doi.org/10.1016/j.cma.2020.113103>.
- Tian, J., Qi, C., Sun, Y. et al. 2020b. Permeability Prediction of Porous Media Using a Combination of Computational Fluid Dynamics and Hybrid Machine Learning Methods. *Engineering with Computers*. <https://doi.org/10.1007/s00366-020-01012-z>.
- Varfolomeev, I., Yakimchuk, I., and Safonov, I. 2019. An Application of Deep Neural Networks for Segmentation of Microtomographic Images of Rock Samples. *Computers* **8** (4): 72. <https://doi.org/10.3390/computers8040072>.
- Wang, Y. D., Blunt, M. J., Armstrong R. T. et al. 2021. Deep Learning in Pore Scale Imaging and Modeling. *Earth-Science Reviews*. **215**: 103555. <https://doi.org/10.1016/j.earscirev.2021.103555>.
- Wang, Y. D., Armstrong, R. T., and Mostaghimi, P. 2020. Boosting Resolution and Recovering Texture of 2D and 3D Micro-CT Images with Deep Learning. *Water Resour Res* **56** (1): e2019WR026052. <https://doi.org/10.1029/2019WR026052>.
- Wang, Y. D., Armstrong, R. T., and Mostaghimi, P. 2019a. Enhancing Resolution of Digital Rock Images with Super Resolution Convolutional Neural Networks. *J Pet Sci Eng* **182**: 106261. <https://doi.org/10.1016/j.petrol.2019.106261>.
- Wang, Y. D., Chung, T., Armstrong, R. T. et al. 2019b. Accelerated Computation of Relative Permeability by Coupled Morphological and Direct Multi-phase Flow Simulation. *J Comput Phys* **401**: 108966. <https://doi.org/10.1016/j.jcp.2019.108966>.
- Wang, Y. D., Chung, T., Armstrong, R. T. et al. 2019c. Computations of Permeability of Large Rock Images by Dual Grid Domain Decomposition. *Adv Water Resour* **126**: 1–14. <https://doi.org/10.1016/j.advwatres.2019.02.002>.
- White, J. A., Borja, R. I., and Fredrich, J. T. 2006. Calculating the Effective Permeability of Sandstone with Multiscale Lattice Boltzmann/Finite Element Simulations. *Acta Geotech* **1** (4): 195–209. <https://doi.org/10.1007/s11440-006-0018-4>.
- Wu, Z., Shen, C., and Van Den Hengel, A. 2019. Wider or Deeper: Revisiting the Resnet Model for Visual Recognition. *Pattern Recognit* **90**: 119–133. <https://doi.org/10.1016/j.patcog.2019.01.006>.
- Xie, S., Girshick, R., Dollár, P. et al. 2017. Aggregated Residual Transformations for Deep Neural Networks. Paper presented at the IEEE Conference on Computer Vision and Pattern Recognition, Honolulu, Hawaii, USA, 21–26 July. <https://doi.org/10.1109/CVPR.2017.634>.
- Yang, X., Mehmani, Y., Perkins, W. A. et al. 2016. Intercomparison of 3D Pore-Scale Flow and Solute Transport Simulation Methods. *Adv Water Resour* **95**: 176–189. <https://doi.org/10.1016/j.advwatres.2015.09.015>.
- Zhang, Q., Cui, Z., Niu, X. et al. 2017. Image Segmentation with Pyramid Dilated Convolution Based on ResNet and U-Net. In *Neural Information Processing. ICONIP 2017. Lecture Notes in Computer Science*, ed. D. Liu, S. Xie, Y. Li, D. Zhao, and E. S. El-Alfy, Vol. 10635, 364–372. Cham, Switzerland: Springer.